

# Engineering Oxygen Vacancies in a Polysulfide-Blocking Layer with Enhanced Catalytic Ability

Zhaohuai Li, Cheng Zhou, Junhui Hua, Xufeng Hong, Congli Sun, Hai-Wen Li, Xu Xu,\* and Liqiang Mai\*


The practical application of the lithium–sulfur (Li–S) battery is seriously restricted by its shuttle effect, low conductivity, and low sulfur loading. Herein, first-principles calculations are conducted to verify that the introduction of oxygen vacancies in TiO<sub>2</sub> not only enhances polysulfide adsorption but also greatly improves the catalytic ability and both the ion and electron conductivities. A commercial polypropylene (PP) separator decorated with TiO<sub>2</sub> nanosheets with oxygen vacancies (OVs-TiO<sub>2</sub>@PP) is fabricated as a strong polysulfide barrier for the Li–S battery. The thickness of the OVs-TiO<sub>2</sub> modification layer is only 500 nm with a low areal mass of around 0.12 mg cm<sup>-2</sup>, which enhances the fast lithium-ion penetration and the high energy density of the whole cell. As a result, the cell with the OVs-TiO<sub>2</sub>@PP separator exhibits a stable electrochemical behavior at 2.0 C over 500 cycles, even under a high sulfur loading of 7.1 mg cm<sup>-2</sup>, and an areal capacity of 5.83 mAh cm<sup>-2</sup> remains after 100 cycles. The proposed strategy of engineering oxygen vacancies is expected to have wide applications in Li–S batteries.

With the rapid consumption of petroleum and other natural energy resources, an energy shortage has become a critical global challenge. An urgent need exists for new energy storage systems with a high capacity, low cost, and environmental soundness. The lithium–sulfur (Li–S) battery with a high theoretical capacity (1675 mAh g<sup>-1</sup>) and energy density (2600 Wh kg<sup>-1</sup>)

Z. H. Li, C. Zhou, J. H. Hua, X. F. Hong, Dr. X. Xu, Prof. L. Q. Mai  
State Key Laboratory of Advanced Technology for Materials Synthesis  
and Processing  
International School of Materials Science and Engineering  
Wuhan University of Technology  
Wuhan 430070, Hubei, P. R. China  
E-mail: xuxu@whut.edu.cn; mlq518@whut.edu.cn

Dr. C. L. Sun  
International School of Materials Science and Engineering  
Nanostructure Research Centre (NRC)  
Wuhan University of Technology  
Wuhan 430070, Hubei, P. R. China

Prof. H.-W. Li  
Platform of Inter/Transdisciplinary Energy Research  
International Research Center for Hydrogen Energy  
International Institute for Carbon-Neutral Energy Research  
Kyushu University  
Fukuoka 819-0395, Japan

 The ORCID identification number(s) for the author(s) of this article can be found under <https://doi.org/10.1002/adma.201907444>.

DOI: 10.1002/adma.201907444

avoids the restriction imposed by the cathode capacity not matching the anode in the lithium-ion battery (LIB).<sup>[1,2]</sup> However, the practical application of the Li–S battery is hindered by low sulfur conductivity ( $5 \times 10^{-30}$  S cm<sup>-1</sup> at room temperature) and large volume expansion (80%) during lithiation.<sup>[3,4]</sup> The most urgent and serious problem to be solved is the shuttle effect, which is caused by the intermediate polysulfide species (Li<sub>2</sub>S<sub>n</sub>,  $4 \leq n \leq 8$ ) dissolving in the electrolyte and commuting between two electrodes, resulting in a low sulfur utilization and a rapid capacity decay.<sup>[5–7]</sup> Furthermore, the last stage of the reaction during the discharging process is a solid phase reaction of the Li<sub>2</sub>S<sub>2</sub> transforming into Li<sub>2</sub>S with sluggish kinetics. The discharging production Li<sub>2</sub>S is easy to attach on the lithium metal anode surface, which has been proved to be a significant factor in the termination of the cell life,

especially under high sulfur loading (>2 mg cm<sup>-2</sup>).<sup>[8–11]</sup>

The separator is an important part of the cell and plays a critical role in determining its electrochemical performance.<sup>[12]</sup> In the past decade, strenuous efforts have been undertaken to investigate various functional separators for preventing the polysulfide shuttle effect, thereby promoting the development of the Li–S battery. Manthiram and Chung were the first to construct a carbon-coated separator for the high-performance Li–S battery.<sup>[13,14]</sup> It is believed that modification of the commercial separator is an efficient means of constructing functional separators. This approach is more convenient and cost effective than the sophisticated design and fabrication of sulfur cathode.<sup>[15–22]</sup> Furthermore, metal oxides have attracted considerable attention as functional materials for separator modification.<sup>[23–26]</sup> However, owing to their intrinsically low electrical conductivity and poor catalytic ability, metal oxides fail to promote the conversion of polysulfides.<sup>[27]</sup> Moreover, to achieve better inhibition of polysulfide dissolution, the modification layer is usually thick, which is undesirable for the fast insertion/deinsertion of Li ions. This places a severe burden on the weight of the whole cell, resulting in a poor rate capability and low energy density.<sup>[28]</sup> In addition, the modified functional separator should be structurally compatible with the requirements of percolating Li-ion conducting pathway and low electrolyte permeability.<sup>[29]</sup>

Building defects (oxygen or sulfur defects) in special-purpose materials plays an important role in energy storage/conversion

system.<sup>[30]</sup> In particular, it comprises a highly effective approach to developing catalysts and powerful inhibitors in the Li-S battery, combining excellent electrical conductivity and catalytic properties for fast polysulfide conversion.<sup>[31–33]</sup> Herein, titanium dioxide with oxygen vacancies (OVs-TiO<sub>2</sub>) was selected for demonstration purposes. First-principles calculations were performed to fully prove that the existence of oxygen vacancies significantly enhances the binding ability to polysulfides and possesses desirable lithium-ion conductivity. Next, an OVs-TiO<sub>2</sub> nanosheets decorated polypropylene (PP) separator (OVs-TiO<sub>2</sub>@PP) was fabricated as a strong polysulfide barrier for the Li-S battery. First, the OVs-TiO<sub>2</sub> inherited the strong chemical adsorption of polysulfides and provided abundant suspended unsaturated bonds at the sites of oxygen defects on the TiO<sub>2</sub> surface, which further enhanced the chemical adsorption to polysulfides. Second, only a small amount of OVs-TiO<sub>2</sub> (around 0.12 mg cm<sup>-2</sup>) was required to construct the functional separator, which benefited the fast Li-ion penetration and high energy density of the cell. Last but not least, the introduction of oxygen vacancies not only enhanced the polysulfide adsorption, but also greatly improved the TiO<sub>2</sub> catalytic ability and conductivity.<sup>[34]</sup> Therefore, OVs-TiO<sub>2</sub> can promote the conversion of

long-chain polysulfides adsorbed on the surfaces to short-chain polysulfides and ensure the high utilization of intermediate products, greatly improving the battery capacity and stability.

Density function theory (DFT) calculations were performed to investigate the OVs-TiO<sub>2</sub> chemical characteristics. When an oxygen vacancy was created on the original TiO<sub>2</sub> (O-TiO<sub>2</sub>) surface (101), the optimized molecular structure of the OVs-TiO<sub>2</sub> was obviously different from that of O-TiO<sub>2</sub> around the site of oxygen vacancy (Figure S1, Supporting Information). The oxygen atoms (O<sub>2</sub> and O<sub>3</sub>) moved toward the oxygen vacancy, equilibrating the uneven electron cloud density on the OVs-TiO<sub>2</sub> surface, as well as the neighboring Ti atoms (Ti<sub>1</sub>–Ti<sub>5</sub>). The oxygen vacancy generation increased the OVs-TiO<sub>2</sub> polarity, which was conducive to capturing polar charged polysulfides. As a result, the corresponding binding energies of OVs-TiO<sub>2</sub> to Li<sub>2</sub>S<sub>3</sub>, Li<sub>2</sub>S<sub>4</sub>, Li<sub>2</sub>S<sub>5</sub>, Li<sub>2</sub>S<sub>6</sub>, Li<sub>2</sub>S<sub>7</sub>, and Li<sub>2</sub>S<sub>8</sub> (Figure 1a) were 3.09, 2.10, 2.27, 2.25, 1.63, and 1.86 eV, respectively (Figure 1b). These energies were much higher than those of O-TiO<sub>2</sub> (1.96, 1.61, 1.29, 1.75, 1.22, and 1.39 eV; Figures S2 and S3, Supporting Information).

As a functional separator in the Li-S battery, the polysulfide blocking ability with a modification layer is easily improved.

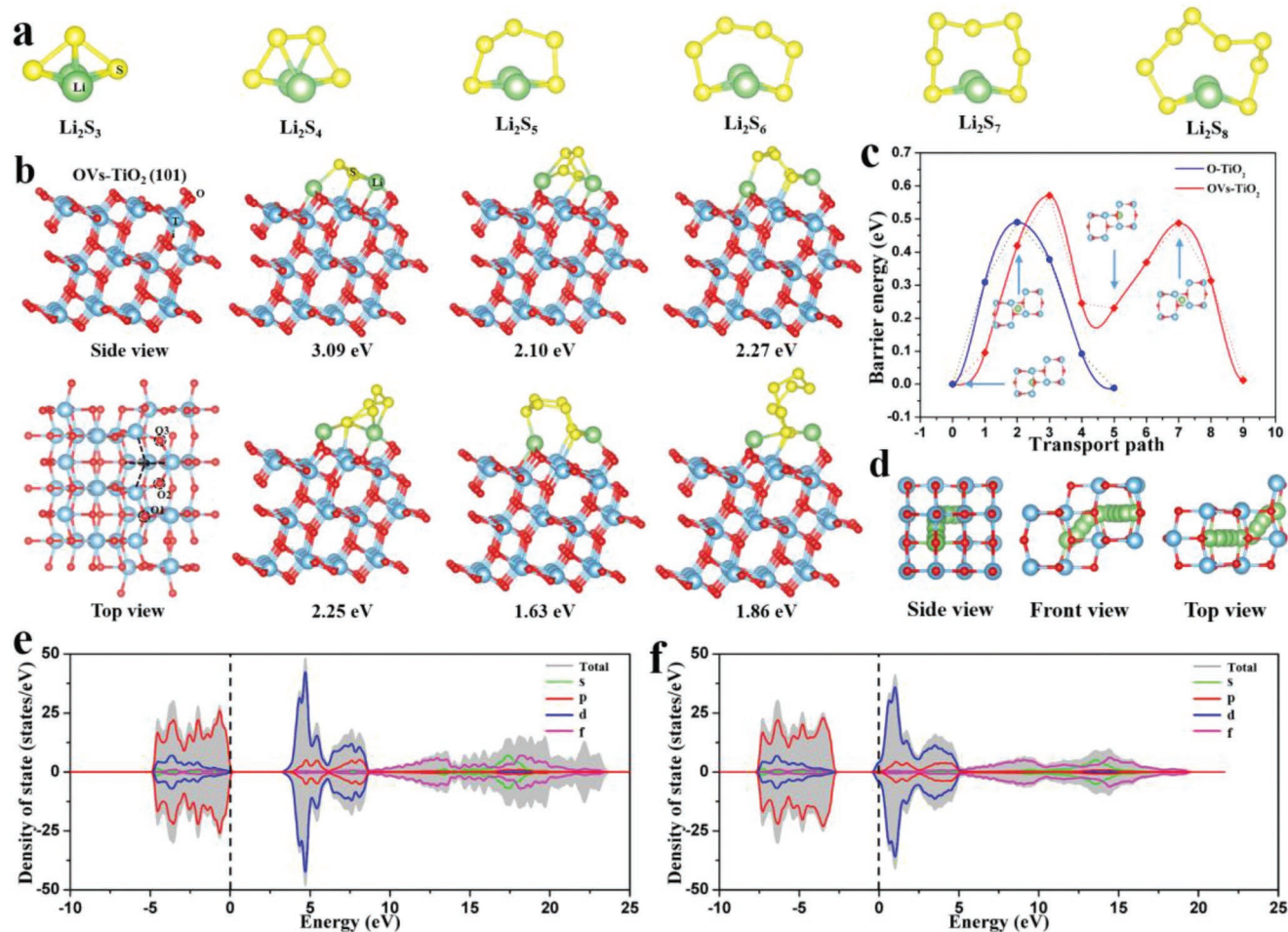


**Figure 1.** DFT calculations. a) Optimized configurations of polysulfides (Li<sub>2</sub>S<sub>x</sub>, 3 ≤ x ≤ 8). b) Optimized configurations of Li<sub>2</sub>S<sub>x</sub> binding to OVs-TiO<sub>2</sub>. c) Energy barrier curves of lithium-ion migration in O-TiO<sub>2</sub> and OVs-TiO<sub>2</sub>. d) Schematic of the Li-transport path in OVs-TiO<sub>2</sub>. e, f) Density of states of O-TiO<sub>2</sub> and OVs-TiO<sub>2</sub>.

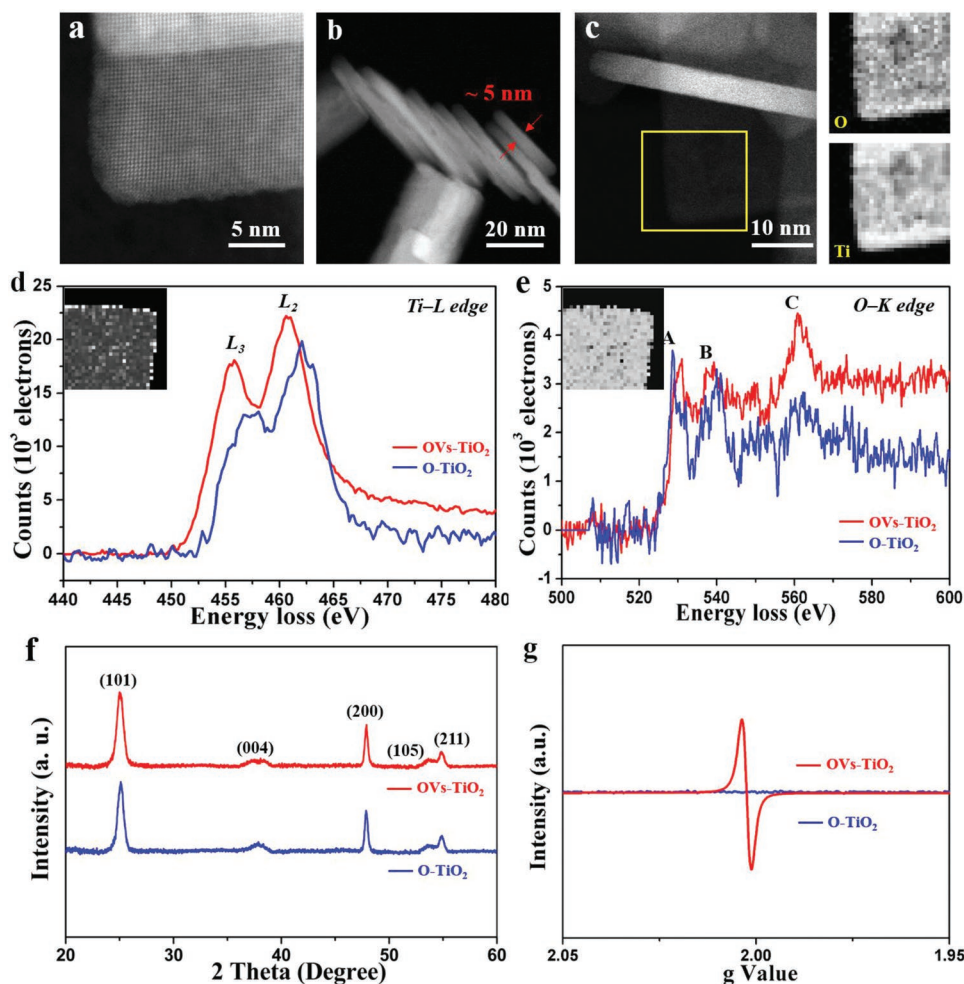


**Figure 2.** Morphological and structural characterizations of OV-TiO<sub>2</sub>. a,b) STEM. c) STEM mappings on the atomic level. d) EELS of the Ti-L edge. e) EELS of the O-K edge. f) XRD patterns of the OV-TiO<sub>2</sub> and O-TiO<sub>2</sub>. g) EPR curves of OV-TiO<sub>2</sub> and O-TiO<sub>2</sub>.

However, this extra layer can engender certain obstacles to the migration of Li ions. To investigate the diffusion behavior of Li ions in O-TiO<sub>2</sub> and OV-TiO<sub>2</sub>, the possible penetration pathway was considered (Figure 1d and Figure S4, Supporting Information). In addition, the energy profile along the migration route was calculated using the climbing-image-nudged elastic band (CINEB) method implemented in the Vienna Ab Initio Simulation Package (VASP) (Figure 1c). As observed in the figures, with the extended migration path, the Li ions migration barrier in OV-TiO<sub>2</sub> decreases as low as that of O-TiO<sub>2</sub>, indicating that the Li ions can effortlessly migrate in OV-TiO<sub>2</sub> during cycling. Figure 1e,f and Figure S5 (Supporting Information) show the density of states for O-TiO<sub>2</sub> and OV-TiO<sub>2</sub>, indicating that the oxygen vacancy presence significantly alters the distribution of valence electrons of the TiO<sub>2</sub> nanosheets. Furthermore, the oxygen atoms near the oxygen vacancy site compensate for the deficiency of the original energy band structure, causing the conduction band to move toward the Fermi level. The increased conductivity and bonding strength are attributed to the oxygen vacancy presence, and the result is well consistent with the calculated binding energies.

Figure 2a presents an atomic-resolution magnified scanning transmission electron microscopy (STEM) image of a single

OV-TiO<sub>2</sub> nanosheet. It clearly depicts the interlacing of Ti and O atoms, indicating good crystallinity. Figure 2b shows that the OV-TiO<sub>2</sub> nanosheets thickness is only 5 nm. The scanning electron microscopy (SEM) and transmission electron microscopy (TEM) images of OV-TiO<sub>2</sub> further prove that the lateral size of the OV-TiO<sub>2</sub> nanosheet is nearly 50 nm with a thin thickness (Figure S6, Supporting Information). The ultrathin OV-TiO<sub>2</sub> nanosheet not only facilitates the generation of oxygen defects, but also benefits the strong adhesion to the PP separator. The high-resolution TEM (HRTEM) and inset image of OV-TiO<sub>2</sub> show the lattice fringes corresponding to the *d*<sub>101</sub> interplanar spacing (*d*<sub>101</sub> = 0.354 nm) of TiO<sub>2</sub> (Figure S6d, Supporting Information). Figure 2c shows the OV-TiO<sub>2</sub> STEM electron energy loss spectroscopy (EELS) mappings, which exhibit the distribution of Ti and O at the atomic level. To investigate more information about the oxygen vacancies, EELS analyses were employed on a single OV-TiO<sub>2</sub> and O-TiO<sub>2</sub> nanosheet, where the Ti-L and O-K edges were simultaneously recorded.<sup>[35]</sup> As shown in Figure 2d, the Ti-L edges can provide more detailed chemical information of OV-TiO<sub>2</sub>. It is clearly observed that the Ti-L edge has a significant deviation of  $\approx 2.4 \pm 0.1$  excess e<sup>-</sup> on the Ti<sup>4+</sup> sites compared with O-TiO<sub>2</sub>. This apparent shift in

the oxygen-bonding environment (Ti–O–Ti) on the surface can be attributed to the oxygen vacancies. Furthermore, the intensity ratio between the OV<sub>s</sub>-TiO<sub>2</sub> L3 and L2 peaks (L3/L2 ratio) is larger than that of O-TiO<sub>2</sub>, indicating a lower Ti oxidation state of OV<sub>s</sub>-TiO<sub>2</sub> compared to O-TiO<sub>2</sub>.<sup>[36]</sup> Figure 2e presents EELS spectra of the O-K edges. The difference between OV<sub>s</sub>-TiO<sub>2</sub> and O-TiO<sub>2</sub> is found to be sensitive to the Ti oxidation state (peaks A, B, and C). This finding further assumes that the shift in Ti-L edges is due to OV<sub>s</sub>-TiO<sub>2</sub> oxygen vacancies. X-ray powder diffraction (XRD) patterns (Figure 2f) suggest the typical structure of the anatase phase (JCPDS No. 21-1272) for both OV<sub>s</sub>-TiO<sub>2</sub> and O-TiO<sub>2</sub>.<sup>[37]</sup> Figure 2g displays the electron paramagnetic resonance (EPR) characterization curves, which verify the defects of the oxygen vacancies. The OV<sub>s</sub>-TiO<sub>2</sub> curve shows an oxygen vacancy signal at the g value of 2.001, whereas O-TiO<sub>2</sub> shows almost no sign of oxygen deficiency. X-ray photoelectron spectroscopy (XPS) spectra were used to investigate the surface defects of O-TiO<sub>2</sub> and OV<sub>s</sub>-TiO<sub>2</sub>. O 1s core-level XPS spectra of O-TiO<sub>2</sub> and OV<sub>s</sub>-TiO<sub>2</sub> exhibit one peak at 530 eV, which is justified as Ti–O–Ti. Another new peak at 531.5 eV of OV<sub>s</sub>-TiO<sub>2</sub> corresponds to the presence of oxygen vacancies (Figure S7, Supporting Information).<sup>[37]</sup>

Based on the above characteristics of the OV<sub>s</sub>-TiO<sub>2</sub> nanosheets, an OV<sub>s</sub>-TiO<sub>2</sub>@PP separator was fabricated as a functional barrier for the Li–S battery. The mechanism is illustrated in Figure 3a–c. The diffuent intermediate polysulfides easily permeate the PP separator with a weak polysulfides obstruction. They are finally reduced to Li<sub>2</sub>S, which is deposited on the lithium anode surface, leading to the low utilization of active material. Moreover, the solid phase Li<sub>2</sub>S layer further hinders the diffusion of lithium ions, resulting in “dead

lithium” and a potential cell failure. In contrast, as OV<sub>s</sub>-TiO<sub>2</sub> has a strong adsorption and excellent catalytic effect on polysulfides, OV<sub>s</sub>-TiO<sub>2</sub>@PP can act as a tenacious barrier to prevent polysulfides from passing through to the lithium anode. This is similar to reservoir-blocking polysulfides in the sulfur cathode. As shown in Figure 3d,e, the OV<sub>s</sub>-TiO<sub>2</sub> nanosheets are uniformly distributed on the PP separator. The side view of the OV<sub>s</sub>-TiO<sub>2</sub>@PP (Figure 3f) illustrates that the thickness of the OV<sub>s</sub>-TiO<sub>2</sub> modification layer is around 500 nm and the areal mass is only 0.12 mg cm<sup>-2</sup>. To ensure polysulfide adsorption, the proportion of the OV<sub>s</sub>-TiO<sub>2</sub> layer should be reduced as far as possible to reduce the weight of the whole battery and ensure its high energy density. The elemental mappings show that OV<sub>s</sub>-TiO<sub>2</sub> nanosheets uniformly coat the PP separator (Figure S8, Supporting Information). Furthermore, the electrolyte wetting properties of the functional separator are important in determining the battery electrochemical performance. Figure S9 (Supporting Information) presents photographs obtained by placing the same amount of electrolyte onto the PP separator and the OV<sub>s</sub>-TiO<sub>2</sub>@PP separator, respectively. The contact angle between the electrolyte/PP separator is as large as 46° and that of electrolyte/OV<sub>s</sub>-TiO<sub>2</sub>@PP separator is 14°. This finding demonstrates the better contact and smaller surface tension of the electrolyte/OV<sub>s</sub>-TiO<sub>2</sub>@PP separator interface, which enhances the wetting and preservation of the electrolyte during cycling. The diffusion of polysulfides across the separator was investigated based on a simple proton exchanger (Figure S10, Supporting Information). The polysulfide solution (0.05 M Li<sub>2</sub>S<sub>6</sub>) was slowly added to the two exchangers. The O-TiO<sub>2</sub>@PP separator and the PP separator were measured under the same conditions. Figure S10 (Supporting

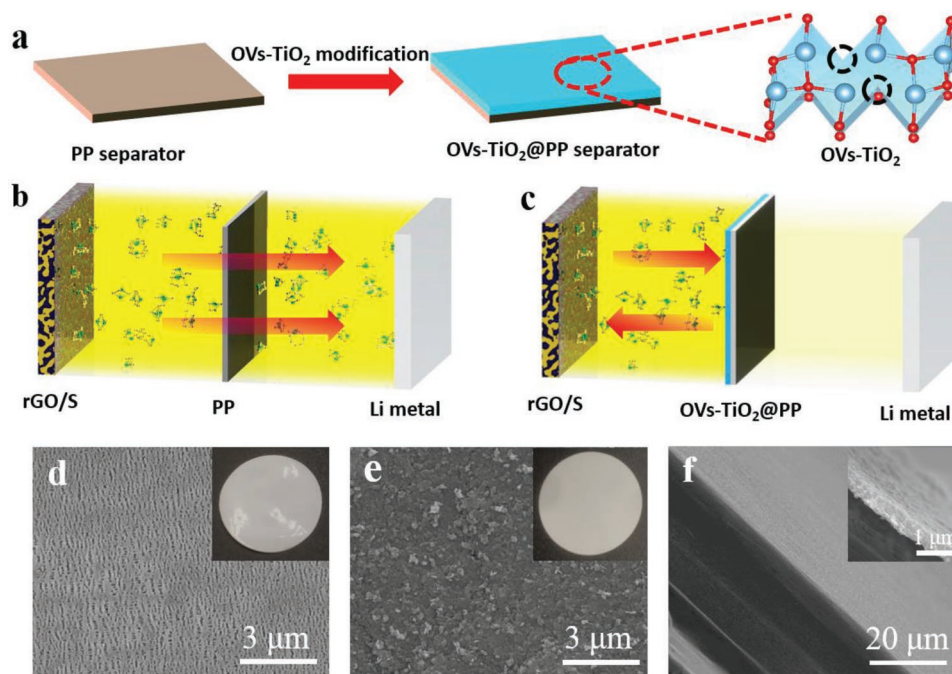


**Figure 3.** Schematic of fabrication and morphology of the OV<sub>s</sub>-TiO<sub>2</sub>@PP separator. a) Schematic of the fabrication of the OV<sub>s</sub>-TiO<sub>2</sub>@PP separator. b,c) Mechanism for inhibiting the shuttle effect of the PP separator and OV<sub>s</sub>-TiO<sub>2</sub>@PP separator. d,e) SEM images of the PP separator and OV<sub>s</sub>-TiO<sub>2</sub>@PP separator. (The insets of (d) and (e) depict optical images of the PP separator and OV<sub>s</sub>-TiO<sub>2</sub>@PP separator, respectively.) f) Cross section of the OV<sub>s</sub>-TiO<sub>2</sub>@PP separator.

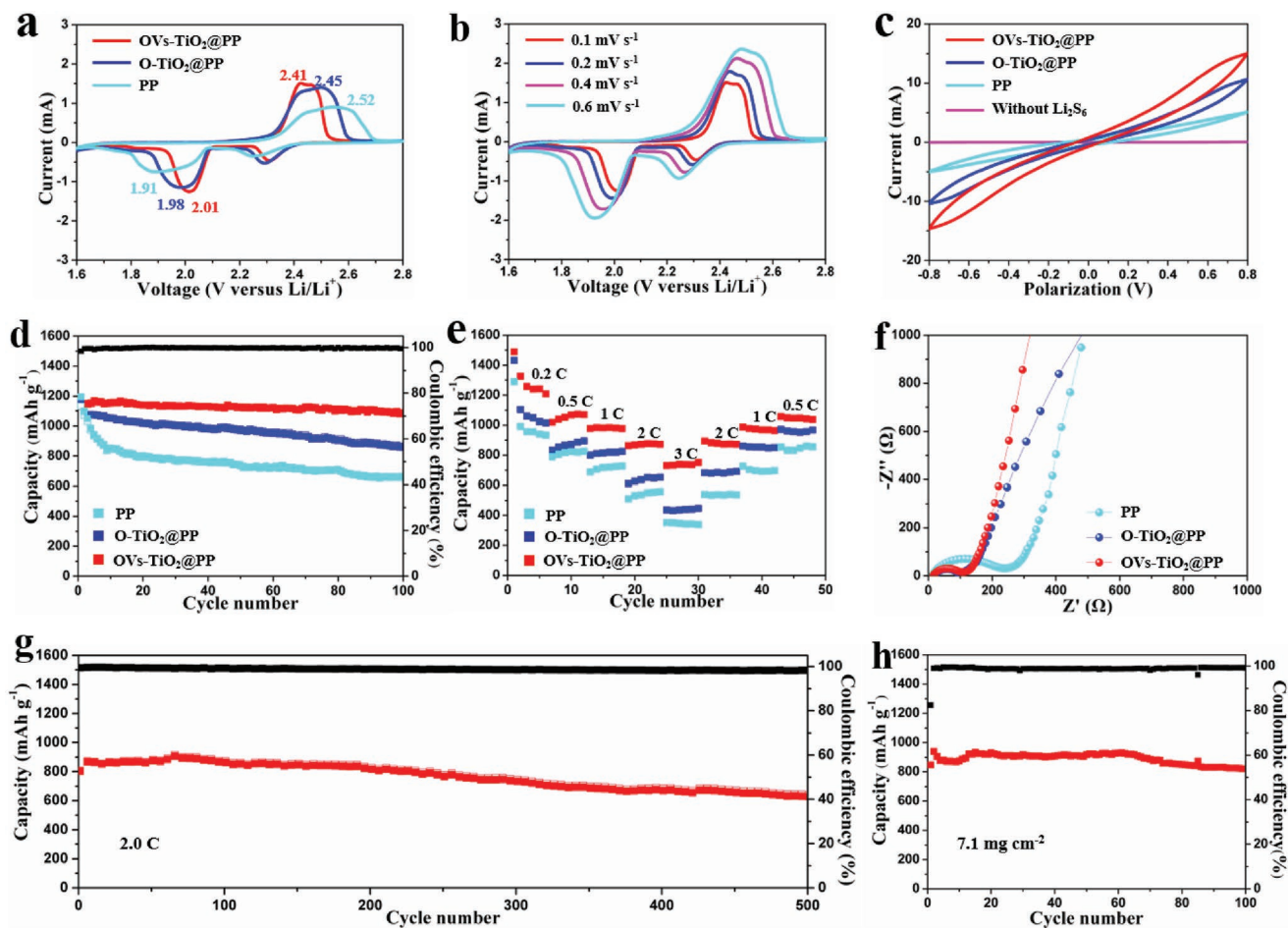


**Figure 4.** Electrochemical performance of the OV<sub>3</sub>-TiO<sub>2</sub>@PP separator and control samples. a) CV curves. b) Multiscan CV curves of the OV<sub>3</sub>-TiO<sub>2</sub>@PP separator. c) CV curves of symmetric cells at 50 mV S<sup>-1</sup>. d) Cycling test at 0.5 C. e) Rate performance. f) EIS test. g) Long-term performance of the OV<sub>3</sub>-TiO<sub>2</sub>@PP separator at a current density of 2.0 C. h) Cycling stability under high sulfur loading.

Information) shows that the PP separator has slight infiltration only when the proton exchanger is sealed. Furthermore, the Li<sub>2</sub>S<sub>6</sub> solution underwent persistent permeation through the separator until the reddish-brown Li<sub>2</sub>S<sub>6</sub> solution completely filled the blank electrolyte within 6 h. The O-TiO<sub>2</sub>@PP separator also displayed significant permeation of the Li<sub>2</sub>S<sub>6</sub> solution within 18 h. In contrast, the Li<sub>2</sub>S<sub>6</sub> species did not easily penetrate the OV<sub>3</sub>-TiO<sub>2</sub>@PP separator, and it remained resistant even after 18 h. This finding further demonstrates that the OV<sub>3</sub>-TiO<sub>2</sub>@PP separator has the best ability to block polysulfides compared to the respective O-TiO<sub>2</sub> and PP separators.

To illustrate the advantages of the OV<sub>3</sub>-TiO<sub>2</sub>@PP separator in the Li-S battery, button cell (CR2025) was assembled in an argon glove box with the OV<sub>3</sub>-TiO<sub>2</sub>@PP separator and the reduced graphene oxide loaded with sulfur (rGO/S) as the working electrode (the sulfur loading was 3.6 mg cm<sup>-2</sup>). The O-TiO<sub>2</sub>@PP separator and PP separator were also prepared for the comparison. The initial cyclic voltammetry (CV) curves of the OV<sub>3</sub>-TiO<sub>2</sub>@PP, O-TiO<sub>2</sub>@PP, and PP separators at a scan rate of 0.1 mV S<sup>-1</sup> are shown in **Figure 4a**. Two reduction peaks are observed on the discharge curve. They are located at 2.02 and 2.32 V of OV<sub>3</sub>-TiO<sub>2</sub>@PP, corresponding to the formation

of long-chain polysulfides and the final Li<sub>2</sub>S product, respectively. The oxidation potential on the charge curve is 2.45 V, which corresponds to the conversion of Li<sub>2</sub>S to sulfur. With respect to the two control samples, the reduction potential of the O-TiO<sub>2</sub>@PP and PP separators deviates significantly from the theoretical reduction potential of the Li-S battery. Their distinct difference of reduction peaks compared to the OV<sub>3</sub>-TiO<sub>2</sub>@PP separator strongly indicates the improved polysulfide redox kinetics by OV<sub>3</sub>-TiO<sub>2</sub>. The initial three CV curves of OV<sub>3</sub>-TiO<sub>2</sub>@PP at a scan rate of 0.2 mV s<sup>-1</sup> are shown in Figure S11a (Supporting Information). There is no obvious difference in the shapes of the three curves, indicating a stable electrochemical reaction inside the battery. Figure 4b and Figure S11b,c (Supporting Information) present the multiscan CV curves of cells with the OV<sub>3</sub>-TiO<sub>2</sub>@PP, OV<sub>3</sub>-TiO<sub>2</sub>@PP, and PP separators. The OV<sub>3</sub>-TiO<sub>2</sub>@PP separator shows a peak current of 1.2 mA at a scan rate of 0.1 mV s<sup>-1</sup>, which is higher than those of the O-TiO<sub>2</sub>@PP (1.1 mA) and PP separators (0.75 mA). This indicates that the OV<sub>3</sub>-TiO<sub>2</sub>@PP separator has a better ion diffusion ability under the low scan rate, which is conducive to polysulfide transformation. However, with the scan rate up to 0.6 mV s<sup>-1</sup>, the three separator types show a comparable peak

current (2 mA). This finding is mainly owing to the OV<sub>s</sub>-TiO<sub>2</sub> modified layer extending the distance by which the Li ions penetrate the separator. In addition, it is clearly observed that, with the increase of the scan rates, the cell with the OV<sub>s</sub>-TiO<sub>2</sub>@PP separator only shows a slight deviation of 0.09 V from 0.1 to 0.6 mV s<sup>-1</sup>. On the contrary, the O-TiO<sub>2</sub>@PP and PP separators show serious polarization with the higher offsets of 0.21 and 0.15 V, respectively. It is thus crucial to evaluate the performance of the Li-S battery by a self-discharge test. As shown in Figure S11d (Supporting Information), the cell with the OV<sub>s</sub>-TiO<sub>2</sub>@PP separator shows only a slight voltage drop of 0.003 V over 24 h, whereas cells with the O-TiO<sub>2</sub>@PP and PP separators show larger voltage drops of 0.007 and 0.021 V, respectively. The results prove that the OV<sub>s</sub>-TiO<sub>2</sub> layer can stabilize the internal reaction and prevent an accidental loss of active material. Figure 4c shows that the current response of the OV<sub>s</sub>-TiO<sub>2</sub>@PP symmetrical cell with Li<sub>2</sub>S<sub>6</sub> is much higher than those of the O-TiO<sub>2</sub>@PP and PP separators. It is further proved that OV<sub>s</sub>-TiO<sub>2</sub>@PP separator facilitates the redox reaction of polysulfides.<sup>[38]</sup> The cycling performances of the OV<sub>s</sub>-TiO<sub>2</sub>@PP, O-TiO<sub>2</sub>@PP, and PP separators at 0.5 C are shown in Figure 4d. A high initial discharge capacity of 1148 mAh g<sup>-1</sup> is obtained with the OV<sub>s</sub>-TiO<sub>2</sub>@PP separator, and 1084 mAh g<sup>-1</sup> remains with a high capacity retention of 94.4% after 100 cycles. In contrast, the O-TiO<sub>2</sub>@PP and PP separators deliver high initial discharge capacities of 1164 and 1195 mAh g<sup>-1</sup>, respectively. However, only 858 and 644 mAh g<sup>-1</sup> remain after 100 cycles. The corresponding capacity retentions are as low as 73.7% and 53.9%, respectively, implying unsatisfactory adsorption and low utilization of active materials. The corresponding Coulombic efficiencies of the OV<sub>s</sub>-TiO<sub>2</sub>@PP, O-TiO<sub>2</sub>@PP, and PP separators are 98.43%, 90.59%, and 90.76%, respectively, for the first cycle, and 99.52%, 98.77%, and 98.55% for the 100th cycle, respectively. These findings demonstrate that the Coulombic efficiency is improved by the OV<sub>s</sub>-TiO<sub>2</sub>@PP separator. In addition, the Coulombic efficiencies of the O-TiO<sub>2</sub>@PP and PP separators greatly fluctuate during cycling, whereas that of the OV<sub>s</sub>-TiO<sub>2</sub>@PP separator is rather stable. The above results are attributed to the enhanced adsorption and catalytic conversion by OV<sub>s</sub>-TiO<sub>2</sub>. Figure S11e (Supporting Information) depicts the cycling performance of the OV<sub>s</sub>-TiO<sub>2</sub>@PP separator at 1.0 C, showing that the OV<sub>s</sub>-TiO<sub>2</sub>@PP separator has a stable cycling ability and high capacity under both low and high current densities.

The rate performances of the OV<sub>s</sub>-TiO<sub>2</sub>@PP, O-TiO<sub>2</sub>@PP, and PP separators are shown in Figure 4e. The OV<sub>s</sub>-TiO<sub>2</sub>@PP separator shows the reversible capacities of 1208, 1069, 977, 872, and 751 mAh g<sup>-1</sup> at the current density from 0.2 to 0.5, 1, 2, and 3 C, respectively. When the current density decreases to 0.5 C, an almost reversible capacity of 1160 mAh g<sup>-1</sup> is recovered with an indistinguishable capacity loss. The O-TiO<sub>2</sub>@PP and PP separators exhibit low capacities at the same rates, especially when the current density increases to 3 C, and only 445 and 339 mAh g<sup>-1</sup> can be retained, respectively. The results show that OV<sub>s</sub>-TiO<sub>2</sub>@PP separator has a strong catalytic capacity; that is, it can quickly catalyze the polysulfide conversion. Additionally, the introduction of oxygen vacancies can provide fast transfer channels for both ions and electrons. The charge-discharge curves (Figure S11f, Supporting

Information) of the OV<sub>s</sub>-TiO<sub>2</sub>@PP separator under different current densities demonstrate that, even under a high current density, the discharge curves still have two obvious discharge platforms, indicating mild polarization within the battery. Electrochemical impedance spectra (EIS) were consulted to elucidate deeper information inside the battery (Figure 4f). As shown in the figure, the OV<sub>s</sub>-TiO<sub>2</sub>@PP separator exhibits a lithium-ion migration rate comparable to that of the PP separator as well as a small internal resistance ( $R_{ct} = 110 \Omega$ ). Both aspects benefit from the facilitated polysulfide conversion and lead to an ideal electrolyte concentration level. A long-term test was performed to illustrate the cycling stability of the OV<sub>s</sub>-TiO<sub>2</sub>@PP separator at a current density of 2.0 C (Figure 4g). A capacity of 802 mAh g<sup>-1</sup> was achieved in the initial cycle. Additionally, a reversible capacity of 631 mAh g<sup>-1</sup> was obtained after 500 cycles, with a capacity decay of only 0.043% per cycle. This excellent cycling stability was owing to the OV<sub>s</sub>-TiO<sub>2</sub>@PP separator acting as a strong barrier for inhibiting the polysulfide shuttle. Moreover, the intrinsic catalytic ability significantly promotes the polysulfide participation in the reaction. Table S1 (Supporting Information) presents a comparison of various metal-based-coating modified separators and this work for the Li-S battery. It can be concluded that the OV<sub>s</sub>-TiO<sub>2</sub>@PP separator has a relative lighter and thinner modification layer than most others, while having a comparable capacity and cycle stability.

It is worth noting that high sulfur loading is a critical challenge for commercial applications of the Li-S battery. However, only a few high-sulfur loadings were implemented in the separator in previous reports. Although high sulfur loadings were achieved in some studies, the corresponding areal capacities (<4 mAh cm<sup>-2</sup>) were too low to compete with commercial LIBs. In the present study, a high sulfur loading of 7.1 mg cm<sup>-2</sup> was achieved with the OV<sub>s</sub>-TiO<sub>2</sub>@PP separator, which exhibited a gravimetric capacity up to 821 mAh g<sup>-1</sup> and an areal capacity of 5.83 mAh cm<sup>-2</sup> at the current density of 2.38 mA cm<sup>-2</sup> (0.2 C) after 100 cycles (Figure 4h). As shown in the figure, the areal mass of the OV-TiO<sub>2</sub> modification layer is only 1.7% of the areal sulfur loading under this condition, which has almost no negative impact in terms of the total energy density of the whole cell. Even in regular sulfur loading (3.6 mg cm<sup>-2</sup>, 0.2 C), the OV<sub>s</sub>-TiO<sub>2</sub>@PP separator shows a higher areal capacity than commercial LIBs (Figure 5a).<sup>[26,27,29,39-45]</sup> Furthermore, the OV<sub>s</sub>-TiO<sub>2</sub>@PP separator has the highest areal capacity of the metal-based modified separators to date (Figure 5b). This attribute greatly strengthens the competitiveness and potential use of functional separators in practical applications.

To verify the blocking ability of OV<sub>s</sub>-TiO<sub>2</sub> on polysulfides, the OV<sub>s</sub>-TiO<sub>2</sub>@PP separator was characterized by SEM and TEM mappings after cycling (Figures S13 and S14, Supporting Information). The mappings show that a large number of polysulfides are adsorbed on the surface of the OV<sub>s</sub>-TiO<sub>2</sub> nanosheets after cycling, and the ability of OV<sub>s</sub>-TiO<sub>2</sub> to strengthen the polysulfide binding is further proved.

In conclusion, polysulfide adsorption and the catalytic ability of TiO<sub>2</sub> were successfully enhanced in this study by engineering oxygen vacancies. Moreover, the PP separator was modified by an OV<sub>s</sub>-TiO<sub>2</sub> modification layer with a thickness

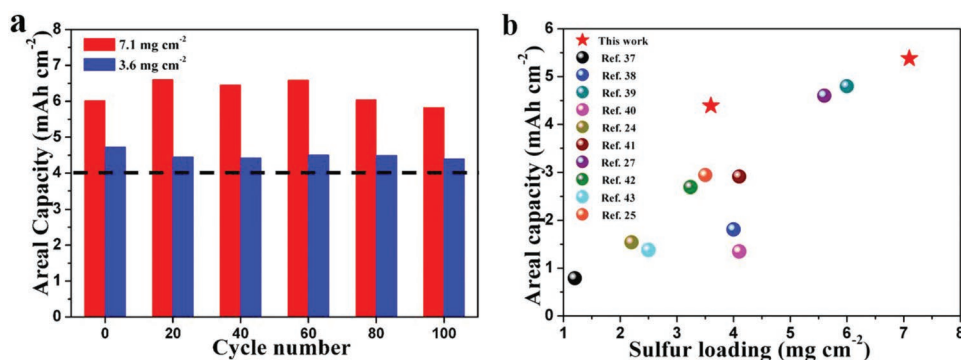


**Figure 5.** a) Comparison of batteries with OVs-TiO<sub>2</sub>@PP separator with commercial LIB in terms of areal capacity. b) Comparison of sulfur loading and areal capacity with various metal-based materials modified separators.

of around 500 nm. The DFT calculations were performed to analyze the advantages of OVs-TiO<sub>2</sub> in depth, showing that OVs-TiO<sub>2</sub> has a better adsorption ability on polysulfides as well as excellent ionic conductivity. Furthermore, the oxygen vacancies greatly enhanced the ability to catalyze the conversion of soluble long-chain polysulfides. STEM-EELS analysis played a key role in confirming the oxygen vacancies in OVs-TiO<sub>2</sub>. Accordingly, the OVs-TiO<sub>2</sub>@PP separator showed a persistent cycling stability under the high current density of 2.0 C over 500 cycles. Even with sulfur loading of 7.1 mg cm<sup>-2</sup>, a high areal capacity of 5.83 mAh cm<sup>-2</sup> was retained after 100 cycles. In sum, it is contended that oxygen vacancies can foster new development opportunities for high-energy-density Li-S batteries or other applications, while providing outstanding prospects for applications of various transition-metal oxides.

## Supporting Information

Supporting Information is available from the Wiley Online Library or from the author.

## Acknowledgements

This work was supported by the National Natural Science Foundation of China (51702247, 51832004), the National Key Research and Development Program of China (2018YFB0104200), the National Natural Science Fund for Distinguished Young Scholars (51425204), the Yellow Crane Talent (Science & Technology) Program of Wuhan City and the Fundamental Research Funds for the Central Universities (WUT: 2019III174, 2018IVB034, 2018IVA088, 2018III025), and the Basic Research Expense of the State Key Laboratory (20131d0005). The S/TEM work was performed at the Nanostructure Research Center (NRC), which was supported by the Fundamental Research Funds for the Central Universities (WUT: 2019III012GX), the State Key Laboratory of Advanced Technology for Materials Synthesis and Processing, and the State Key Laboratory of Silicate Materials for Architectures (all of the laboratories are at Wuhan University of Technology). The State Key Laboratory of Advanced Technology for Materials Synthesis and Processing (WUT:2019-KF-5, 2020-KF-3).

## Conflict of Interest

The authors declare no conflict of interest.

## Keywords

catalytic ability, lithium-sulfur batteries, oxygen vacancies

Received: November 12, 2019

Revised: December 23, 2019

Published online: January 29, 2020

- [1] X. L. Ji, K. T. Lee, L. F. Nazar, *Nat. Mater.* **2009**, *8*, 500.
- [2] P. G. Bruce, S. A. Freunberger, L. J. Hardwick, J. M. Tarascon, *Nat. Mater.* **2012**, *11*, 19.
- [3] L. B. Ma, W. J. Zhang, L. Wang, Y. Hu, G. Y. Zhu, Y. R. Wang, R. P. Chen, T. Chen, Z. X. Tie, J. Liu, Z. Jin, *ACS Nano* **2018**, *12*, 4868.
- [4] J. H. Kim, Y. H. Lee, S. J. Cho, J. G. Gwon, H. J. Cho, M. Jang, S. Y. Lee, S. Y. Lee, *Energy Environ. Sci.* **2019**, *12*, 177.
- [5] L. Luo, S.-H. Chung, H. Y. Asl, A. Manthiram, *Adv. Mater.* **2018**, *30*, 1804149.
- [6] C. Ye, Y. Jiao, H. Jin, A. D. Slattery, K. Davey, H. H. Wang, S.-Z. Qiao, *Angew. Chem., Int. Ed.* **2018**, *57*, 16703.
- [7] D. R. Deng, F. Xue, C.-D. Bai, J. Lei, R. M. Yuan, M. S. Zheng, Q. F. Dong, *ACS Nano* **2018**, *12*, 11120.
- [8] J. Xie, B.-Q. Li, H.-J. Peng, Y.-W. Song, M. Zhao, X. Chen, Q. Zhang, J.-Q. Huang, *Adv. Mater.* **2019**, *31*, 1903813.
- [9] Y. Liu, Y. Qiao, Y. Zhang, Z. Yang, T. T. Gao, D. Kirsch, B. Y. Liu, J. W. Song, B. Yang, L. B. Hu, *Energy Storage Mater.* **2018**, *12*, 197.
- [10] L. B. Ma, R. P. Chen, Y. Hu, W. J. Zhang, G. Y. Zhu, P. Y. Zhao, T. Chen, C. X. Wang, W. Yan, Y. R. Wang, L. Wang, Z. X. Tie, J. Liu, Z. Jin, *Energy Storage Mater.* **2018**, *14*, 258.
- [11] Y. Zhong, D. L. Chao, S. G. Deng, J. Y. Zhan, R. Y. Fang, Y. Xia, Y. D. Wang, X. L. Wang, X. H. Xia, J. P. Tu, *Adv. Funct. Mater.* **2018**, *9*, 1706391.
- [12] C. H. Chang, S.-H. Chung, S. Nanda, A. Manthiram, *Mater. Today Energy* **2017**, *6*, 72.
- [13] S.-H. Chung, A. Manthiram, *Adv. Mater.* **2014**, *26*, 7352.
- [14] S.-H. Chung, A. Manthiram, *Adv. Funct. Mater.* **2014**, *24*, 5299.
- [15] G. M. Zhou, L. Li, D.-W. Wang, X.-Y. Shan, S. F. Pei, F. Li, H.-M. Cheng, *Adv. Mater.* **2015**, *27*, 641.
- [16] H. J. Peng, D. W. Wang, J. Q. Huang, X. B. Cheng, Z. Yuan, F. Wei, Q. Zhang, *Adv. Sci.* **2016**, *3*, 1500268.
- [17] T. Z. Zhuang, J. Q. Huang, H. J. Peng, L. Y. He, X. B. Cheng, C. M. Chen, Q. Zhang, *Small* **2016**, *12*, 381.
- [18] S. Y. Bai, X. Z. Liu, K. Zhu, S. C. Wu, H. S. Zhou, *Nat. Energy* **2016**, *1*, 16094.
- [19] J.-H. Kim, G. Y. Jung, Y.-H. Lee, J.-H. Kim, S.-Y. Lee, S. K. Kwak, S.-Y. Lee, *Nano Lett.* **2017**, *17*, 2220.

- [20] Y. Pang, J. S. Wei, Y. G. Wang, Y. Y. Xia, *Adv. Energy Mater.* **2018**, *10*, 1702288.
- [21] J. Sun, Y. M. Sun, M. Pasta, G. M. Zhou, Y. Z. Li, W. Liu, F. Xiong, Y. Cui, *Adv. Mater.* **2016**, *28*, 9797.
- [22] B.-Q. Li, H.-J. Peng, X. Chen, S.-Y. Zhang, J. Xie, C.-X. Zhao, Q. Zhang, *CCS Chem.* **2019**, *1*, 128.
- [23] X. Liu, J.-Q. Huang, Q. Zhang, L. Q. Mai, *Adv. Mater.* **2017**, *29*, 1601759.
- [24] J.-Y. Hwang, H. M. Kim, S.-K. Lee, J.-H. Lee, A. Abouimrane, M. A. Khaleel, I. Belharouak, A. Manthiram, Y.-K. Sun, *Adv. Energy Mater.* **2016**, *6*, 1501480.
- [25] S. Imtiaz, Z. A. Zafar, R. Razaq, D. Sun, Y. Xin, Q. Li, Z. L. Zhang, L. Zheng, Y. H. Huang, J. A. Anderson, *Adv. Mater.* **2018**, *5*, 1800243.
- [26] N. X. Shi, B. J. Xi, Z. Y. Feng, F. F. Wu, D. H. Wei, J. Liu, S. L. Xiong, *J. Mater. Chem. A* **2019**, *7*, 4009.
- [27] Y. Z. Song, W. Zhao, L. Kong, L. Zhang, X. Y. Zhu, Y. L. Shao, F. Ding, Q. Zhang, J. Y. Sun, Z. F. Liu, *Energy Environ. Sci.* **2018**, *11*, 2620.
- [28] J. R. He, Y. F. Chen, A. Manthiram, *Energy Environ. Sci.* **2018**, *11*, 2560.
- [29] Z. A. Ghazi, X. He, A. M. Khattak, N. A. Khan, B. Liang, A. Iqbal, J. X. Wang, H. Sin, L. S. Li, Z. Y. Tang, *Adv. Mater.* **2017**, *29*, 1606817.
- [30] S. J. Deng, Y. Zhang, D. Xie, P. L. Yang, G. Z. Wang, X. S. Zheng, J. F. Zhu, X. L. Wang, Y. Yu, G. X. Pan, X. H. Xia, J. P. Tu, *Nano Energy* **2019**, *4*, 355.
- [31] Y. K. Wang, R. F. Zhang, J. Chen, H. Wu, S. Y. Lu, K. Wang, H. L. Li, C. J. Harris, K. Xi, R. V. Kumar, S. J. Ding, *Adv. Energy Mater.* **2019**, *9*, 1900953.
- [32] H.-E. Wang, K. L. Yin, N. Qin, X. Zhao, F.-J. Xia, Z.-Y. Hu, G. L. Guo, G. Z. Cao, W. J. Zhang, *J. Mater. Chem. A* **2019**, *7*, 10346.
- [33] H.-C. Wang, C.-Y. Fan, Y.-P. Zheng, X.-H. Zhang, W.-H. Li, S.-Y. Liu, H.-Z. Sun, J.-P. Zhang, L.-N. Sun, X.-L. Wu, *Chem. - Eur. J.* **2017**, *23*, 9666.
- [34] E. H. M. Salhabi, J. L. Zhao, J. Y. Wang, M. Yang, B. Wang, D. Wang, *Angew. Chem., Int. Ed.* **2019**, *58*, 9078.
- [35] Z. L. Wang, J. S. Yin, Y. D. Jiang, *Micron* **2000**, *31*, 571.
- [36] M. Nord, P. E. Vullum, M. Moreau, J. E. Boschker, S. M. Selbach, R. Holmestad, T. Tybell, *Appl. Phys. Lett.* **2015**, *106*, 041604.
- [37] J. W. Wan, W. X. Chen, C. Y. Jia, L. R. Zheng, J. C. Dong, X. S. Zheng, Y. Wang, W. S. Yan, C. Chen, Q. Peng, D. S. Wang, Y. D. Li, *Adv. Mater.* **2018**, *30*, 1705369.
- [38] X.-J. Hong, C.-L. Song, Y. Yang, H.-C. Tan, G.-H. Li, Y.-P. Cai, H. X. Wang, *ACS Nano* **2019**, *13*, 1923.
- [39] Z. B. Xiao, Z. Yang, L. Wang, H. G. Nie, M. Zhong, Q. Q. Lai, X. J. Xu, L. J. Zhang, S. M. Huang, *Adv. Mater.* **2015**, *27*, 2891.
- [40] F. Q. Lia, G. C. Wang, P. Wang, J. Yang, K. Zhang, Y. X. Liu, Y. Q. Lai, *J. Electroanal. Chem.* **2017**, *788*, 150.
- [41] F. Liu, Q. F. Xiao, H. B. Wu, F. Sun, X. Y. Liu, F. Li, Z. Y. Le, L. Shen, G. Wang, M. Cai, Y. F. Lu, *ACS Nano* **2017**, *11*, 2697.
- [42] Y. Q. Lai, P. Wang, F. R. Qin, M. Xu, J. Li, K. Zhang, Z. A. Zhang, *Energy Storage Mater.* **2017**, *9*, 179.
- [43] L. Kong, H.-J. Peng, J.-Q. Huang, W. C. Zhu, G. Zhang, Z.-W. Zhang, P.-Y. Zhai, P. P. Sun, J. Xie, Q. Zhang, *Energy Storage Mater.* **2017**, *8*, 153.
- [44] X. X. Chen, X. Y. Ding, C. S. Wang, Z. Y. Feng, L. Q. Xu, X. Gao, Y. J. Zhai, D. B. Wang, *Nanoscale* **2018**, *10*, 13694.
- [45] X. Song, G. P. Chen, S. Q. Wang, Y. P. Huang, Z. Y. Jiang, L.-X. Ding, H. H. Wang, *ACS Appl. Mater. Interfaces* **2018**, *10*, 26274.